HHS Public Access

Author manuscript

Cancer Res. Author manuscript; available in PMC 2022 September 01.

Published in final edited form as:

Cancer Res. 2022 March 01; 82(5): 859–871. doi:10.1158/0008-5472.CAN-21-2376.

IgA-dominated humoral immune responses govern patients' outcome in endometrial cancer

Gunjan Mandal[1], **Subir Biswas**[1], **Carmen M. Anadon**[1], **Xiaoqing Yu**[2], **Chandler D. Gatenbee**[3], **Sandhya Prabhakaran**[3], **Kyle K. Payne**[1], **Ricardo A. Chaurio**[1], **Alexandra Martin**[1], **Patrick Innamarato**[1], **Carlos Moran**[4], **John J. Powers**[1], **Carly M. Harro**[1], **Jessica A. Mine**[1], **Kimberly B. Sprenger**[1], **Kristen E. Rigolizzo**[1], **Xuefeng Wang**[2], **Tyler J. Curiel**[5], **Paulo C. Rodriguez**[1], **Alexander R. Anderson**[3], **Ozlen Saglam**[4], **Jose R. Conejo-Garcia**[1,*]

[1]Department of Immunology, H. Lee Moffitt Cancer Center & Research Institute, Tampa, FL 33612, USA.

[2]Department of Biostatistics and Bioinformatics, H. Lee Moffitt Cancer Center & Research Institute, Tampa, FL 33612, USA.

[3]Department of Mathematical Oncology, H. Lee Moffitt Cancer Center & Research Institute, Tampa, FL 33612, USA.

[4]Department of Pathology, H. Lee Moffitt Cancer Center & Research Institute, Tampa, FL 33612, USA.

[5]Mays Cancer Center, University of Texas Health, San Antonio, TX 78229, USA.

Abstract

Recent studies suggest that B cells could play an important role in the tumor microenvironment. However, the role of humoral responses in endometrial cancer remains insufficiently investigated. Using a cohort of 107 patients with different histological subtypes of endometrial carcinoma, we evaluated the role of coordinated humoral and cellular adaptive immune responses in endometrial cancer. Concomitant accumulation of T, B, and plasma cells at tumor beds predicted better survival. However, only B cell markers corresponded with prolonged survival specifically in high-grade endometrioid type and serous tumors. Immune protection was associated with class-switched IgA and, to a lesser extent, IgG. Expression of polymeric immunoglobulin receptor (pIgR) by tumor cells and its occupancy by IgA were superior predictors of outcome and correlated with defects in methyl directed DNA mismatch repair. Mechanistically, pIgR-dependent, antigen-independent IgA occupancy drove activation of inflammatory pathways associated with IFN and TNF signaling in tumor cells, along with apoptotic and ER stress

[*]**CORRESPONDENCE**: José R Conejo-Garcia, MD, PhD, H. Lee Moffitt Cancer Center and Research Institute, 12902 Magnolia Drive, Tampa, FL 33612, jose.conejo-garcia@moffitt.org, Phone: (813) 745-8282, Fax: (813) 745-5580.

AUTHORS' CONTRIBUTIONS

Conceptualization: GM, SB, OS and JRCG; Methodology: GM, SB, CMA, YX, CG, SP, KKP, RAC, AM, PI, CM, JJP, CMH, JAM, KBS, KER, WX; Investigation: GM, SB, PCR, OS and JRCG; Formal Analysis: GM, SB, JRCG; Writing: GM, SB, YX, TJC, ARA, JRCG; Review and Editing: All authors;

Conflict of Interest statement

JRCG has stock options in Compass Therapeutics, Anixa Biosciences and Alloy Therapeutics; has sponsored research with Anixa Biosciences; receives honorarium from Alloy Theraputics and Leidos; and has intellectual property with Compass Therapeutics and Anixa Biosciences.

pathways, while thwarting DNA repair mechanisms. Together, these findings suggest that coordinated humoral and cellular immune responses, characterized by IgA:pIgR interactions in tumor cells, determine the progression of human endometrial cancer as well as the potential for effective immunotherapies.

INTRODUCTION

Spontaneous immune responses in epithelial cancers are associated with improved patients' outcome (1–4). Although most studies focus on uncovering the predictive value of T cells, recent studies support the importance of B cell infiltrations in the tumor microenvironment, suggesting that T cell responses do not work in isolation (4–7).

The role of B cells in the tumor microenvironment has been associated with both the production of antibodies against tumor antigens (5,8), and their capacity to present antigens (9). Antibodies can bind to the antigens or receptors on cancer cells and promote antibody-dependent cell-mediated cytotoxicity/phagocytosis (5,10,11). At least, some epithelial cancer cells express the receptor for polymeric IgM or IgA antibodies, polymeric immunoglobulin receptor (pIgR) (5,12–16). pIgR expression has been correlated with opposite disease prognosis in multiple cancers, including hepatocellular cancer and ovarian cancer (5,13,16). We recently showed that the binding and subsequent transcytosis of IgA antibodies through ovarian cancer cells promote MHC independent T cell-mediated killing of cancer cells, probably by the upregulation of interferon receptors (5). However, the immune landscape of endometrial cancer, which is one of the major cancer types in women across the world (17,18), remains incompletely understood.

In an effort to identify likely responders to different clinical interventions, endometrial carcinomas have been recently re-classified based on genomic features (19). Some of these clasifications include mutation-induced DNA repair gene dysfunction, which are typically associated with increased cancer risk. For instance, an individual with a germline mutation in one or more of the methyl directed DNA mismatch repair (MMR) genes such as *MLH1*, *MSH2*, *MSH6* or *PMS2* is more susceptible to colorectal cancer, endometrial cancer (20,21) and possibly, breast cancer (22), prostate cancer (23), pancreatic cancer (22), and cancers at many other locations (21). Accordingly, the immunogenicity of endometrial cancer was recently evaluated in terms of MMR defects in endometrial cancer patients (24).

In this study, we evaluated the elusive role of coordinated humoral and cellular adaptive immune responses in endometrial cancer, including the extent of class-switched IgA and IgG antibodies production across multiple histological subtypes. Our results indicate that coordinated B cell and T cell responses predict superior survival of endometrial cancer patients. Humoral responses are dominated by IgA in most patients, and its occupancy of pIgR in tumor cells is a major predictor of improved patient survival.

MATERIALS AND METHODS

Human endometrial cancer tissue microarrays

We have analyzed two Tissue Microarrays (TMA) procured from Moffitt Cancer Center Tissue Core Facility, each of which include endometrial cancer tissues (n = 107, total; clear cell- n = 18 endometrioid type high grade (grade 3)- n = 28; endometrioid type low grade- n = 30; serous- n = 31) and some control tissues. The study protocol was approved by the institutional review board at the Moffitt Cancer Center. Individual tissue blocks were reviewed to confirm histology and grade and make TMAs. Lymph node contamination was ruled out. TMAs were arrayed using 1 mm sized needle and by taking two duplicate core biopsies from endometrial cancer tissue blocks or control tissues, and re-embedding the cores into a single block.

Multiplex Immunofluorescence and Immunohistochemistry Staining Procedure

FFPE TMAs were immunostained using the PerkinElmer OPAL TM 7-Color Automation IHC kit (Waltham, MA) on the BOND RX autostainer (Leica Biosystems, Vista, CA) and the following anti-human antibodies: CD3 (Dako, A0452), CD4 (Cell Marque, EP204, 104R-25), CD8 (Dako, C8/144B, M7103,), CD19 (Dako, LE-CD19, M7296), CD138 (Dako, MI15, M7228), pIgR (Abcam, ab96196), IgA (Abcam, EPR5367–76, ab124716), IgG (Abcam, EPR4421, ab109489) and pan Cytokeratin (PCK, Dako, AE1/AE3, M3515). Nuclei were stained with DAPI. Precisely, tissues were baked at 65°C for 2 hours then transferred to the BOND RX (Leica Biosystems) followed by automated deparaffinization, antigen retrieval using OPAL IHC procedure (PerkinElmer). Autofluorescence slides (negative control) were included, which use primary and secondary antibodies omitting the OPAL fluors. Slides were scanned and imaged with the PerkinElmer Vectra®3 Automated Quantitative Pathology Imaging System. Multi-layer TIFF images were exported from InForm (PerkinElmer) and loaded into HALO (Indica Labs, New Mexico) for quantitative image analysis. Each fluorescent fluorophore is assigned to a dye color and positivity thresholds were determined per marker based on published nuclear or cytoplasmic staining patterns. Quantitation in tumor islets and stroma were distinguished by PCK staining. Datasets were exported with cytoplasmic, nuclear and total cell counts for each fluorescent marker from the sample set.

DNA repair molecules were independently stained using a Ventana Discovery XT automated system (Ventana Medical Systems, Tucson, AZ) as per manufacturer's protocol with proprietary reagents for MLH1 (M1, #790–5091, Ventana), MSH2 (G219–1129, #790–5093, Ventana), MSH6 (BC/44, CM265A, Biocare) and PMS2 (EPR3947, ab110638, Abcam) antibodies. The expression of these markers was evaluated by using 1% cut-off level. If any one of duplicate cores had 1% nuclear staining, the MMR protein was considered as "preserved".

Optimization of multiplex immunofluorescence and immunohistochemistry staining experiments with appropriate positive and negative control tissues, including isotype control antibodies, are summarized in Supplementary Fig.S1. Sections of human tonsil tissues were used as a positive control for CD3, CD4, CD8, CD19, CD138, IgA, IgG and PCK, and

as a negative control for pIgR. Sections of healthy kidney tissues were used as a positive control for pIgR. Sections of Glioblastoma tissues were used as a negative control for CD3, CD4, CD8, CD19, CD138, IgA, IgG and PCK. Respective isotype control antibodies to rule out false-positive staining. Sections of human colon adenocarcinoma tissues were used as positive control for MLH1, MSH2, MSH6, PMS2.

Image processing and spatial analysis

Image registration-—Each sample core had two slices taken in close proximity, each of which was stained using a different panel of markers. The DAPI channel was extracted from each slice's image and used to align the two slices as follows: 1) Each image's features were detected using BRISK, and then described with the VGG feature descriptor (25); 2) features were matched using brute force, and the matched features subsequently used to find the similarity matrix, M, that can warp the matched features to align with one another; 3) M was used to apply a rigid transformation to the image; 4) The rigid alignments were improved using a non-rigid transformation, using the deformation fields (dx, dy) found using Deep Optical Flow (26). The positions of each cell could then be warped using these same transformations. All image registration was conducted in Python 3.7.

Spatial association networks-—Using the image registration parameters (M, dx, dy) that aligned to the two images, the position of each cell was warped such that they also aligned. Spatial association networks were then found for the subset of samples that had an alignment error less than 25μm. First, each TMA core was divided into 100μm x 100μm quadrats, and the of number of each cell type was counted within each quadrat. The ecoCopula package for R was then used to find the spatial association network for each core (27). An average association network for each histological type was then created from the individual networks. The averaged spatial associations were then clustered using the Leiden community detection algorithm (one graph of average positive associations and second graph of average negative associations) (28). Spatial communities contain cell types (i.e. "nodes") that have strong spatial associations with one another (i.e. are "densely connected"), and weaker and/or negative spatial associations with other communities (i.e. are "loosely connected"). Grouping cell types into communities based on their spatial associations help to better understand the overall spatial structure of the tumor, as cells in one community tend to be found co-localized with one another, and potentially isolated from other communities. Combined with understanding of how cell types interact mechanistically (e.g. cytotoxic T-cells preying upon tumor cells), we can treat each community as a functional group. This, in turn, paints a bigger picture of the spatial interactions within the tumor, facilitating a better understanding of how and why cells are interacting with one another.

Summary of spatial patterns-—As image registration was not cell-cell perfect, summaries of spatial relationships based on cell positions (as opposed to quadrat counts) used the original un-warped cell positions. As such, each panel of markers was analyzed independently. Significance of departures from complete spatial randomness (CSR) was determined using the Diggle-Cressie-Loosmore-Ford (DCLF) test on the cross-type L-function for homogeneous point patterns (i.e. Besag's transformation of Ripley's K

function) (29). Clustering was considered significant when $p \leq 0.05$ for the alternative hypothesis of "greater", i.e., there were more cells within a radius r than expected under CSR. If the two-sided alternative hypothesis could not be rejected, the spatial pattern for sample was defined as CSR. Fisher's exact test for count data was used to determine if the number of samples with clustering was significantly different between each pairwise combination of histological types.

In addition to determining if there was significant clustering between pairs of phenotypes, we used simulation envelopes of the cross-type L-function to determine at which distances clustering is observed. In each core, the envelopes for each phenotype pair were determined using 100 simulated realizations of CSR, as described in (30). Distances at which significant clustering occurred were those where the observed cross-type L-function was greater than the upper envelope. Points where the observed cross-type L-function fell between the lower and upper envelopes were considered to be associated with complete spatial randomness (CSR).

t-distributed Stochastic Neighbor Embedding (t-SNE)-—We extracted cell segments per core to build a count matrix with cells as rows and known phenotypes as columns. The known phenotypes are defined as follows: Cytotoxic T cell: $DAPI^+/CD3^+/CD8^+/CD4^-/CD19^-/CD138^-$, Helper T cell: $DAPI^+/CD3^+/CD4^+/CD8^-/CD19^-/CD138^-$, Non-Plasma B cell: $DAPI^+/CD19^+/CD138^-/CD3^-/CD4^-/CD8^-$, Plasma cell: $DAPI^+/CD19^+/CD138^+/CD3^-/CD4^-/CD8^-$, IgG: $DAPI^+/IgG^+/IgA^-/pIgR^-/CD19^-/CD138^-$, IgA: $DAPI^+/IgA^+/IgG^-/pIgR^-/CD19^-/CD138^-$, pIgR: $DAPI^+/pIgR^+/IgA^-/IgG^-/CD19^-/CD138^-$.

A Euclidean distance matrix of dimension cells x cells is generated from this count matrix to compute the neighboring cells for each cell. We then build a spatial neighborhood for each cell where the phenotype expression of each cell is the average of six of its spatially-nearest neighbors in Euclidean space. This approach is inspired by the cellular neighborhoods in (31).

Cells along with their spatial neighbors from all the cores are merged and clustered using a Gaussian mixture model (32) to extract heterogeneous cell types that are also spatially distinct. The differentially-expressed phenotypes used to annotate each cell type are those phenotypes with the highest z-score values for the log-normalized expression per cell type. The cells are further embedded in reduced 2D space using tSNE (33).

Cell line, culture and transduction

HEK-293T, and human endometrial cancer cell lines, KLE and HEC-1-A were procured from ATCC (Manassas, VA). HEK-293T, KLE, and HEC-1-A cells were routinely cultured in RPMI-1640 (Sigma), DMEM/F12 (Gibco), and McCoy's 5A (Thermo) media, respectively, supplemented with 10% FBS, penicillin (100 I.U./ml), streptomycin (100 μg/ml), L-glutamine (2 mM), and sodium pyruvate (0.5 mM) (ThermoScientific). Cell lines were routinely tested for negative mycoplasma contamination. Human *PIGR*-coding sequence was cloned into pLVX-IRES-ZsGreen1 lentiviral vector (Genscript), and virus were produced by co-transfecting with viral packaging plasmids into HEK-293T cells using

Lipofectamine-3000 (Invitrogen). KLE cells were transduced with 0.45μ filtered virus, and checked under microscope for ZsGreen-expression.

Western Blotting

Cells were lysed in RIPA buffer (ThermoScientific) with protease-phosphatase inhibitor cocktail (SigmaAldrich) and cleared by centrifugation. Proteins were quantified by BCA assay (ThermoScientific). Membranes were blotted with anti-pIgR (Abcam, ab96196), CHOP (CST, L63F7, 2895) and anti-β-actin (CST, 13E5, 5125) antibodies.

Fluorescence-activated cell sorting (FACS)

Sorting of $PIGR^{transduced}$ KLE cells were performed by staining with DAPI (ThermoScientific) viability dye, blocking with anti-CD16/32 (BioLegend), and staining for 30 min at 4°C with anti-human pIgR (ThermoScientific, PA5–35340) antibodies, followed by incubation with Alexa Fluor-647-conjugated secondary antibodies (CST). Samples were subsequently FACS sorted using BD FACS ARIA. Data were analyzed using FlowJo.

RNA sequencing

KLE (*wild type* or $PIGR^{transduced}$ overexpressed) and HEC-1-A cell lines in 2% FBS containing DMEM/F12 or McCoy's 5A media, respectively, were treated with or without 0.5 μg/ml of natural human IgA or IgG for 72 hours. Total RNA were isolated from cultured cells using RNA isolation kit (Qiagen) and analyzed for RINe. Next gen RNA sequencing was performed by the Moffitt Cancer Center Molecular Genomics Facility. Paired-end RNA-seq reads were aligned to the GRCh37 human reference genome using STAR (34) (version 2.5.3a) following adaptor trimming by cutadapt (https://doi.org/10.14806/ej.17.1.200) (version 1.8.1). Uniquely mapped reads were counted by featureCounts (35) (version 1.5.3) using Gencode V30 transcript annotations for human. Differential expression analysis was performed using DESeq2 (36). Heat-maps were made using z-score transformed log 2 (1 + normalized count).

For every differential expression analysis comparing antibody treated groups vs. untreated group, genes were ranked based on –log10(p-value)*(sign of log2(fold-change)). The pre-ranked gene list was used to perform pre-ranked gene set enrichment analysis (GSEA version 4.0.2) (37) to assess enrichment of hallmarks, curated gene sets, and gene ontology (38) terms in MSigDB (37). The resulting normalized enrichment score (NES) and FDR controlled p-values were used to assess the IgA-induced transcriptome changes. Pathways have been seclected based on the magnitude of changes among the most significantly altered ones and commonalities of the effects of IgA on both the cell lines, and presented.

Quantitative reverse-transcriptase real-time PCR

RNA was reverse transcribed to cDNAs using SuperScript-IV (Invitrogen) and oligo-dT (Invitrogen). Quantification of human *PIGR*, *CLIP3*, *LAMP3*, *CCL20*, *CCL5*, *TICAM1*, *DDIT3*, *MMP1*, *CEBPG*, *VEGFA*, *ARHGEF2*, *GADD45A*, and *FEN1* mRNA, was performed using SYBR Green mastermix reagent (Applied Biosystems). Expression was normalized by α-tubulin levels. Fold changes relative to average cycle threshold (C_T) values in control samples were calculated by the equation $2^{-\Delta\Delta C_T}$.

Analysis of TCGA data

RNA-seq HTSeq raw count generated from Gencode v22 for The Cancer Genome Atlas Uterine Corpus Endometrial Carcinoma (UCEC) was downloaded from Genomic Data Commons Data Portal (https://portal.gdc.cancer.gov/). Variance stabilization transformation (vsd) implemented in DESeq2 (36) was performed on the raw gene count to create a log2-scaled variance-stabilized gene expression matrix for downstream analyses. Clinical data was obtained from cBio Cancer Genomics Portal (http://www.cbioportal.org/). A total of 528 patients with matched clinical information and tumor RNA-seq data were used in this study. Another detaset of 547 patients with information for mutations or deletions of four MMR genes MLH1, MSH2, MSH6 and PMS2 and overall survival information was downloaded from cBioPortal and used. Pre-calculated RNA-seq based enrichment for 64 immune and stromal cell types was downloaded for TCGA 33 cancer types from xcell (39). Enrichment scores of T cells, B cells, and Plasma cells across TCGA pan-cancer were visualized by boxplots.

Statistical analyses

Unpaired two-tailed non-parametric Mann-Whitney test were performed between two groups, unless indicated otherwise. In addition to Kaplan-Meier plots, Cox regression model has been used for adusting for covaraites, wherever feasible. We limited survival analysis to univariate Mantel-Cox test in occassions where data from a single histology type are used, or between groups with low sample volumes. Analyses were carried out in Graph Pad Prism (v.9.0) or R (v.3.6.1) software. A significance threshold 0.05 for *P* values was used.

DATA AVAILABILITY STATEMENT:

The data generated in this study are available within the article and its supplementary data files. RNA sequencing datasets generated in this study have been deposited in Gene Expression Omnibus (NCBI) under accession number GSE180455.

RESULTS

Humoral response in endometrial cancer is dominated by class-switched IgA antibodies

We recently showed that in serous ovarian cancer, IgA antibodies and, in a lesser extent, IgG responses, govern the magnitude of anti-tumor immunity (5). To understand the role of humoral immunity in endometrial cancer, we stained 107 endometrial cancer specimens from four histological subtypes for expression of IgA and IgG antibodies (Supplementary Fig.S2). Clinicopathological information of tissue specimens are summarized in Table 1. We found similar densities of PCK^+ tumor cells across different histological types (Supplementary Fig.S3A), which were quasi-universally coated by both IgA and IgG (Fig. 1A&B). High-grade endometrioid type tumors showed significantly higher density of IgA and IgG antibodies at PCK^+ tumor islets, compared to other histology types, while clear cell endometrial cancers showed the lowest intra-epithelial IgA and IgG accumulation (Fig. 1B). Notably, virtually all endometrial tumors of any histology expressed pIgR (Supplementary Fig.S2), the IgA/IgM receptor associated with other epithelial cancers (5,40–42). Accordingly, the density of coating of tumor cells by IgA is higher than

IgG-coating in 63% of tumors (Fig. 1A). t-SNE analysis of spatial interactions between different immune markers showed large clusters of PCK^+ tumors cells expressing pIgR, and multiple clusters of IgA and IgG with pIgR-expressing cancer cells (Fig. 1C). The tSNE depicts 90 thousand PCK^+ tumors cells of which the proportion of cells expressing pIgR is 23.6%, pIgR with IgA is 11.7%, pIgR with IgA and IgG is 22.4%, and pIgR with IgG is 33%. These clusters are consistent across all four histology types of endometrial cancer (Supplementary Fig.S3B). Endometrioid type tumors (both high- and low-grade) exhibited higher pIgR expression, compared to serous cancer, while clear cell endometrial tumors showed the lowest pIgR abundance (Fig. 1D). Interestingly, we found that higher $pIgR^+$ cancer cell density predicts improved, albeit not significant, patient survival (Fig.1E, Supplementary Fig.S3C), with corresponding results for *PIGR* mRNA expression in endometrial cancer TCGA dataset ($n = 528$) (Fig.1F, Supplementary Fig.S3C). Most importantly, IgA occupancy of pIgR at tumor cells, rather than mere IgA density, strongly predicts patients' survival (Fig.1G, Supplementary Fig.S3C). As expected, endometrioid type tumors showed the highest percentages of pIgR occupancy by IgA (Fig.1H). Together, these results indicate that, similar to ovarian cancer, IgA production at tumor beds determines endometrial cancer progression through interactions with pIgR, quasi-universally expressed in tumor cells.

Human IgA, but not IgG, alters multiple signaling pathways in $pIgR^+$ endometrial cancer cells in an antigen-independent manner

To understand the effect of IgA binding to pIgR on endometrial cancer cells, we used $pIgR^+$ HEC-1-A endometrial cancer cells, along with pIgR-negative KLE endometrial cancer cells, which we lentivirally transduced with pIgR or mock-transduced (Supplementary Fig.S3D–G). Treatment with irrelevant IgA, but not IgG, induced genome-wide transcriptional changes in both systems in a pIgR-dependent manner (Fig.2A&B, Supplementary Fig.S3H&I). GSEA pathway analyses and subsequent Q-PCR analyses revealed IgA-driven activation of multiple inflammatory pathways, including tumor necrosis factor (TNF)-signaling and interferon production, among other cytokines. Furthermore, pIgR:IgA interactions induced the transcription of multiple genes associated with endoplasmic reticulum (ER)-stress and the unfolded protein response (UPR), which converge in CHOP/DDIT3-mediated apoptosis (Fig.2C&D, Supplementary Fig.S3J&4). In addition, IgA signaling dampened DNA repair pathways in $pIgR^{transduced}$ KLE and $pIgR^+$ HEC-1-A cells (Fig.2C, Supplementary Fig.S3J&4), which positively correlate with the progression of multiple cancer types, and can be targeted with existing and emerging drugs (43–46). Therefore, the favorable prognostic value of pIgR:IgA interactions at tumor beds is determined by the activation of pro-apoptotic and inflammatory pathways in tumor cells, independently of antigen recognition.

Delayed malignant progression is associated with concomitant B- and T- cell infiltration at tumor beds and high density of class-switched antibodies

Recent studies have underscored the importance of B cell activity synchronized with T cell activity at the tumor beds for a sustained, robust anti-tumor humoral response in multiple cancer types (4,5,47,48). To understand the importance of coordinated T cell and B cell responses in the production of IgA and IgG antibodies, and subsequent immune

protection, we also stained our cohort of endometrial cancer patients, along with some healthy endometrium samples, with markers of B and T lymphocytes, and plasma cells (Supplementary Fig.S5). We observed significant infiltration by lymphocytes of both lineages, with distinct t-SNE clusters of cytotoxic T cells, helper T cells, B cells and plasma cells in all histological types of endometrial cancer, consistent with TCGA enrichment scores (Fig.3A, Supplementary Fig.S6). For the 84 thousand cells depicted on the tSNE, the proportion of cytotoxic T cells is 30.2%, helper T cells is 40.5%, plasma cells is 5%, and B cells is 10%. The highest density of T cell and B cell infiltration was found again in high-grade endometrioid type tumors (Fig.3B). Supporting coordinated cellular and humoral adaptive immune responses, B cell infiltration significantly correlated with T cell accumulation (Fig.3C, Supplementary Fig.S7A&B). Accordingly, the densities of IgA and IgG were maximum in tumors where denser concomitant T cell and B cell infiltrates are identified (Fig.3D).

Spatial point pattern analyses revealed important differences in the spatial relationship of cytotoxic and helper T cells with non-plasma B cells. We observe that the serous histology type and endometrioid type low grades exhibited the earliest switch in spatial pattern, transitioning from complete spatial randomness to spatial clustering, starting around 100μm (Fig.4A). However, the distribution of the distances at which spatial clustering was observed between non-plasma and plasma B cells with helper T cells was significantly different between serous type and endometrioid type low grade (Fig.4B). The distribution of clustering distances between non-plasma B-cells and helper T cells also similar between serous and clear cell endometrial tumors, but each of the two types was significantly different compared to low and high grade endometrial cancer (Fig.4B). In contrast, the distribution of clustering distances between non-plasma and plasma B cells with cytotoxic T cells did not differ significantly between serous type and endometrioid type low grade samples (Fig.4B). Interestingly, the only B cell – T cell clustering distribution that differed significanctly between serous and clear cell endometrial tumors was that between non-plasma B-cells and cytotoxic T cells (Fig.4B).

Analysis of the spatial association networks within each histology type in PCK^+ tumor epithelium or in total tumor tissues showed that each histology type has distinct spatial communities, detected by clustering the strength of spatial associations (Fig.4C, Supplementary Fig.S7C). Notably, the tumor epithelium exhibits different spatial communities compared to respective total tumor areas (Fig.4C, Supplementary Fig.S7C). Consistent with the clustering between B cells and T cells, spatial pattern and distribution analyses between IgA and pIgR at varying distances discovered maximum clustering as a function of the distances in the serous type (Fig.4D&E, Supplementary Fig.S7D&E). Consequently, endometrial tumors with increased accumulation of B cells and $CD19^+CD138^+$ plasma cells and, to a lesser extent, T cells, exhibited improved overall survival (Fig.5A–C, Supplementary Fig.S7F–I). Corresponding associations between increased abundance of pan-B cell marker CD19 (a cell surface protein restricted to B cell lymphocytes, and continuously and stably expressed on all stages of B lineage differentiation), and pan-T cell marker CD3, and delayed malignant progression were also identified in 528 patients in endometrial cancer TCGA datasets (Fig.5D&E, Supplementary Fig.S7J). Notably, in high-grade endometrioid type and serous tumors,

superior outcome was associated with infiltration of $CD19^+$ B cells, but not $CD3^+$ T lymphocytes (Supplementary Fig.S8A–D), suggesting a predominant role of antibody-mediated protection in these patients. In contrast, the predictive value of T cells is stronger in clear cell endometrial cancer, compared to B cell accumulation. Together, these data indicate that the production of IgA or IgG is consistently associated with concurrent infiltration of T and B lymphocytes in endometrial cancer, which predicts delayed malignant progression. This is suggestive of coordinated activation of both arms of the adaptive immune system, with a predominant role of humoral *vs.* cellular responses depending on histological subtypes.

Alterations in methyl directed DNA mismatch repair (MMR) pathway genes are associated with higher pIgR-occupancy by IgA in endometrial cancer

Endometrial carcinomas have been recently re-classified based on genomic features (19). To gain additional insight about how defects in MMR proteins influence the immunogenicity of endometrial cancer, we stained our cohort for MLH1, MSH2, MSH6 and PMS2 proteins. Low-grade endometrioid type tumors showed the highest percentage of loss of one or more MMR protein expression (23.33%; $n = 37$), followed by high-grade endometrioid type carcinomas (21.43%; $n = 34$). In contrast, serous and clear cell endometrial cancers showed infrequent loss of MMR protein expression (9.68%; $n = 34$ and 11.11%; $n = 20$, respectively) (Fig.6A). We did not find a significant association between B cell, plasma cell, or T cell infiltration and loss of one or more MMR proteins (Fig.6B–E). However, deregulated MMR protein expression is significantly associated with higher percentages of IgA bound to pIgR (Fig.7A). This is associated with a significant increase in pIgR expression, but not IgA or IgG densities (Fig.7B–D), suggesting an intrinsic property of MMR-deregulated endometrial cancer cells to upregulate pIgR and favor IgA-pIgR interaction. Similar to available TCGA data, combined or individual loss of one or more MMR protein expressions do not predict overall survival (Fig.7E–I, Supplementary Fig.S8E–I).

DISCUSSION

Here we show that coordinated B cell and T cell responses can predict the outcome of patients with endometrial cancer of multiple combined histological subtypes, but only B and plasma cell infiltration predicts survival in patients specifically with serous and high-grade endometrioid type tumors. Humoral responses are dominated by IgA in terms of staining, followed by IgG. Accordingly, pIgR occupancy by IgA in tumor cells is consistently associated with better outcome and elicitiation of pro-apoptotic pathways.

In an effort to inform adjuvant treatment, endometrial carcinomas have been recently re-classified based on molecular features into four categories: POLE ultramutated, microsatellite instability hypermutated, copy-number low, and copy-number high (19). Previous studies reported that immune responses correlate with endometrial cancer molecular subtype but does not carry independent prognostic significance (49). Although these studies did not include the analyses of antibody isotypes and used an alternative molecular classification, we also found a significant correlation between MMR protein

deregulation and higher percentages of IgA bound to pIgR, along with overall increase in pIgR density. Moreover, we found that B and plasma cell infiltration has predictive value in specifically serous and high-grade endometrioid type tumors. In contrast, the outcome of patients with clear cell carcinomas, which were restricted to 5 samples in the aforementioned study (49), depends on tumor-infiltrating T cells, rather than humoral responses. Our study, therefore, suggests that different histological subtypes of endometrial cancer orchestrate different immune responses that spontaneously determine the patients' outcome, but it is also consistent with their dependence on the molecular make-up of each tumor.

A major finding of our study is that, as we reported for other gynecologic malignancies (5), pIgR is quasi-universally expressed in endometrial cancer cells. The highest expression levels correspond to endometrioid type tumors. An exception is the KLE cell line, which allowed us to investigate the effect of pIgR-mediated IgA signaling by restoring pIgR expression. Independently of antigen recognition, irrelevant IgA, but not IgG, elicited an array of inflammatory, ER stress and pro-apoptotic transcriptional pathways in tumor cells. This is consistent with the significant anti-tumor effects of control IgA in $pIgR^+$ ovarian tumors *in vivo* (5), and provides a rationale for testing dimeric IgA as an alternative reagent for immunotherapeutic antibodies in cancer patients. High-grade endometrioid type tumors also showed higher density of both IgA and IgG antibodies coating tumor cells. However, the density of IgA is higher than that of IgG-coating in the majority of tumors. IgA, therefore, dominates the antibody response in endometrial cancer, although IgG responses are also very strong in endometrioid type and serous tumors.

B cells infiltrating most established tumors have been traditionally associated with immunosuppressive activity, through the production of IL-10, IL-35 and/or TGF-β (50). However, a flurry of recent studies in human cancer consistently associates B cell responses with better outcome and concomitant T cell infiltration (5,50). Beyond the elusive role of tertiary lymphoid structures (51), our study suggests that humoral responses, and in particular IgA responses, are as important in many gynecologic tumors as effector T cells. Modulating humoral responses that synergize with existing T cell-centric immunotherapies could pave the way for novel interventions to control aggressive endometrial cancers, which could be applicable to other gynecologic malignancies.

Supplementary Material

Refer to Web version on PubMed Central for supplementary material.

ACKNOWLEDGEMENTS

Support for Shared Resources was provided by Cancer Center Support Grant (CCSG) CA076292 to H. Lee Moffitt Cancer Center. This study was supported by R01CA157664, R01CA124515, R01CA178687 and R01CA211913 to JRCG; R01CA184185 to PCR. KKP was supported by T32CA009140 and The American Cancer Society Postdoctoral Fellowship. CG, SP, and ARA gratefully acknowledge funding from both the Cancer Systems Biology Consortium and the Physical Sciences Oncology Network at the National Cancer Institute, through grants U01CA232382 and U54CA193489 as well as support from the Moffitt Center of Excellence for Evolutionary Therapy. We are especially grateful to CLIA Tissue Imaging Laboratory, Molecular Genomics, Flow Cytometry, Biostatistics and Bioinformatics, Analytic Microscopy Core, and Tissue Core Facility Shared Resources at Moffitt Cancer Center, for exceptional support.

REFERENCES

1. Pan XB, Lu Y, Yao DS. Identification of prognostic tumor-infiltrating immune cells in endometrial adenocarcinoma. Medicine (Baltimore) 2021;100:e26170 [PubMed: 34032778]
2. Liu Y Immune response characterization of endometrial cancer. Oncotarget 2019;10:982–92 [PubMed: 30847026]
3. Zhang L, Conejo-Garcia JR, Katsaros D, Gimotty PA, Massobrio M, Regnani G, et al. Intratumoral T cells, recurrence, and survival in epithelial ovarian cancer. N Engl J Med 2003;348:203–13 [PubMed: 12529460]
4. Helmink BA, Reddy SM, Gao J, Zhang S, Basar R, Thakur R, et al. B cells and tertiary lymphoid structures promote immunotherapy response. Nature 2020;577:549–55 [PubMed: 31942075]
5. Biswas S, Mandal G, Payne KK, Anadon CM, Gatenbee CD, Chaurio RA, et al. IgA transcytosis and antigen recognition govern ovarian cancer immunity. Nature 2021
6. Hollern DP, Xu N, Thennavan A, Glodowski C, Garcia-Recio S, Mott KR, et al. B Cells and T Follicular Helper Cells Mediate Response to Checkpoint Inhibitors in High Mutation Burden Mouse Models of Breast Cancer. Cell 2019;179:1191–206 e21 [PubMed: 31730857]
7. Petitprez F, de Reynies A, Keung EZ, Chen TW, Sun CM, Calderaro J, et al. B cells are associated with survival and immunotherapy response in sarcoma. Nature 2020;577:556–60 [PubMed: 31942077]
8. Garaud S, Buisseret L, Solinas C, Gu-Trantien C, de Wind A, Van den Eynden G, et al. Tumor infiltrating B-cells signal functional humoral immune responses in breast cancer. JCI Insight 2019;5
9. Wennhold K, Thelen M, Lehmann J, Schran S, Preugszat E, Garcia-Marquez M, et al. CD86+ antigen-presenting B cells are increased in cancer, localize in tertiary lymphoid structures, and induce specific T-cell responses. Cancer Immunol Res 2021
10. Hosseini SS, Khalili S, Baradaran B, Bidar N, Shahbazi MA, Mosafer J, et al. Bispecific monoclonal antibodies for targeted immunotherapy of solid tumors: Recent advances and clinical trials. Int J Biol Macromol 2021;167:1030–47 [PubMed: 33197478]
11. Kinker GS, Vitiello GAF, Ferreira WAS, Chaves AS, Cordeiro de Lima VC, Medina TDS. B Cell Orchestration of Anti-tumor Immune Responses: A Matter of Cell Localization and Communication. Front Cell Dev Biol 2021;9:678127 [PubMed: 34164398]
12. Zhou M, Liu C, Cao G, Gao H, Zhang Z. Expression of polymeric immunoglobulin receptor and its biological function in endometrial adenocarcinoma. J Cancer Res Ther 2019;15:420–5 [PubMed: 30964121]
13. Yue X, Ai J, Xu Y, Chen Y, Huang M, Yang X, et al. Polymeric immunoglobulin receptor promotes tumor growth in hepatocellular carcinoma. Hepatology 2017;65:1948–62 [PubMed: 28073159]
14. Qi X, Li X, Sun X. Reduced expression of polymeric immunoglobulin receptor (pIgR) in nasopharyngeal carcinoma and its correlation with prognosis. Tumour Biol 2016;37:11099–104 [PubMed: 26910773]
15. Ohkuma R, Yada E, Ishikawa S, Komura D, Kubota Y, Hamada K, et al. High expression levels of polymeric immunoglobulin receptor are correlated with chemoresistance and poor prognosis in pancreatic cancer. Oncol Rep 2020;44:252–62 [PubMed: 32627041]
16. Ai J, Tang Q, Wu Y, Xu Y, Feng T, Zhou R, et al. The role of polymeric immunoglobulin receptor in inflammation-induced tumor metastasis of human hepatocellular carcinoma. J Natl Cancer Inst 2011;103:1696–712 [PubMed: 22025622]
17. Lortet-Tieulent J, Ferlay J, Bray F, Jemal A. International Patterns and Trends in Endometrial Cancer Incidence, 1978–2013. J Natl Cancer Inst 2018;110:354–61 [PubMed: 29045681]
18. Zhang S, Gong TT, Liu FH, Jiang YT, Sun H, Ma XX, et al. Global, Regional, and National Burden of Endometrial Cancer, 1990–2017: Results From the Global Burden of Disease Study, 2017. Front Oncol 2019;9:1440 [PubMed: 31921687]
19. Cancer Genome Atlas Research N, Kandoth C, Schultz N, Cherniack AD, Akbani R, Liu Y, et al. Integrated genomic characterization of endometrial carcinoma. Nature 2013;497:67–73 [PubMed: 23636398]
20. Dowty JG, Win AK, Buchanan DD, Lindor NM, Macrae FA, Clendenning M, et al. Cancer risks for MLH1 and MSH2 mutation carriers. Hum Mutat 2013;34:490–7 [PubMed: 23255516]

21. Umar A, Boland CR, Terdiman JP, Syngal S, de la Chapelle A, Ruschoff J, et al. Revised Bethesda Guidelines for hereditary nonpolyposis colorectal cancer (Lynch syndrome) and microsatellite instability. J Natl Cancer Inst 2004;96:261–8 [PubMed: 14970275]
22. Win AK, Young JP, Lindor NM, Tucker KM, Ahnen DJ, Young GP, et al. Colorectal and other cancer risks for carriers and noncarriers from families with a DNA mismatch repair gene mutation: a prospective cohort study. J Clin Oncol 2012;30:958–64 [PubMed: 22331944]
23. Grindedal EM, Moller P, Eeles R, Stormorken AT, Bowitz-Lothe IM, Landro SM, et al. Germ-line mutations in mismatch repair genes associated with prostate cancer. Cancer Epidemiol Biomarkers Prev 2009;18:2460–7 [PubMed: 19723918]
24. Willvonseder B, Stogbauer F, Steiger K, Jesinghaus M, Kuhn PH, Brambs C, et al. The immunologic tumor microenvironment in endometrioid endometrial cancer in the morphomolecular context: mutual correlations and prognostic impact depending on molecular alterations. Cancer Immunol Immunother 2021;70:1679–89 [PubMed: 33340331]
25. Simonyan K, Vedaldi A, Zisserman A. Learning Local Feature Descriptors Using Convex Optimisation. IEEE Transactions on Pattern Analysis and Machine Intelligence 2014;36:1573–85 [PubMed: 26353339]
26. Weinzaepfel P, Revaud J, Harchaoui Z, Schmid C. DeepFlow: Large displacement optical flow with deep matching. IEEE Intenational Conference on Computer Vision (ICCV) 2013
27. Team RC. R: A Language and Environment for Statistical Computing. Vienna, Austria: R Foundation for Statistical Computing; 2019.
28. Mucha PJ, Richardson T, Macon K, Porter MA, Onnela JP. Community structure in time-dependent, multiscale, and multiplex networks. Science 2010;328:876–8 [PubMed: 20466926]
29. Lengyel I, Derish P. Ripley BD 1981. Spatial statistics. John Wiley Sons, New York. 2002
30. Baddeley A, Rubak E, Turner R. Spatial Point Patterns: Methodology and Applications with R. London: Chapman and Hall/CRC Press; 2015.
31. Schurch CM, Bhate SS, Barlow GL, Phillips DJ, Noti L, Zlobec I, et al. Coordinated Cellular Neighborhoods Orchestrate Antitumoral Immunity at the Colorectal Cancer Invasive Front. Cell 2020;182:1341–59 e19 [PubMed: 32763154]
32. Deisenroth MP, Faisal AA, Ong CS. Mathematics for machine learning. Cambridge University Press; 2020.
33. Kobak D, Berens P. The art of using t-SNE for single-cell transcriptomics. Nature communications 2019;10:1–14
34. Dobin A, Davis CA, Schlesinger F, Drenkow J, Zaleski C, Jha S, et al. STAR: ultrafast universal RNA-seq aligner. Bioinformatics 2013;29:15–21 [PubMed: 23104886]
35. Liao Y, Smyth GK, Shi W. featureCounts: an efficient general purpose program for assigning sequence reads to genomic features. Bioinformatics 2014;30:923–30 [PubMed: 24227677]
36. Love MI, Huber W, Anders S. Moderated estimation of fold change and dispersion for RNA-seq data with DESeq2. Genome Biol 2014;15:550 [PubMed: 25516281]
37. Subramanian A, Tamayo P, Mootha VK, Mukherjee S, Ebert BL, Gillette MA, et al. Gene set enrichment analysis: a knowledge-based approach for interpreting genome-wide expression profiles. Proc Natl Acad Sci U S A 2005;102:15545–50 [PubMed: 16199517]
38. Ashburner M, Ball CA, Blake JA, Botstein D, Butler H, Cherry JM, et al. Gene ontology: tool for the unification of biology. The Gene Ontology Consortium. Nat Genet 2000;25:25–9 [PubMed: 10802651]
39. Aran D, Hu Z, Butte AJ. xCell: digitally portraying the tissue cellular heterogeneity landscape. Genome Biol 2017;18:220 [PubMed: 29141660]
40. Ocak S, Pedchenko TV, Chen H, Harris FT, Qian J, Polosukhin V, et al. Loss of polymeric immunoglobulin receptor expression is associated with lung tumourigenesis. Eur Respir J 2012;39:1171–80 [PubMed: 21965228]
41. Fristedt R, Elebro J, Gaber A, Jonsson L, Heby M, Yudina Y, et al. Reduced expression of the polymeric immunoglobulin receptor in pancreatic and periampullary adenocarcinoma signifies tumour progression and poor prognosis. PLoS One 2014;9:e112728 [PubMed: 25397670]

42. Dewdney B, Hebbard L. A novel role for polymeric immunoglobulin receptor in tumour development: beyond mucosal immunity and into hepatic cancer cell transformation. Hepatobiliary Surg Nutr 2018;7:52–5 [PubMed: 29531947]
43. Cohen-Eliav M, Golan-Gerstl R, Siegfried Z, Andersen CL, Thorsen K, Ørntoft TF, et al. The splicing factor SRSF6 is amplified and is an oncoprotein in lung and colon cancers. J Pathol 2013;229:630–9 [PubMed: 23132731]
44. Davenne T, Rehwinkel J. PNP inhibitors selectively kill cancer cells lacking SAMHD1. Molecular & cellular oncology 2020;7:1804308 [PubMed: 33235905]
45. Mesquita KA, Ali R, Doherty R, Toss MS, Miligy I, Alblihy A, et al. FEN1 Blockade for Platinum Chemo-Sensitization and Synthetic Lethality in Epithelial Ovarian Cancers. Cancers (Basel) 2021;13 [PubMed: 35008178]
46. Kuroda M, Funasaki S, Saitoh T, Sasazawa Y, Nishiyama S, Umezawa K, et al. Determination of topological structure of ARL6ip1 in cells: identification of the essential binding region of ARL6ip1 for conophylline. FEBS Lett 2013;587:3656–60 [PubMed: 24076029]
47. Cabrita R, Lauss M, Sanna A, Donia M, Skaarup Larsen M, Mitra S, et al. Tertiary lymphoid structures improve immunotherapy and survival in melanoma. Nature 2020;577:561–5 [PubMed: 31942071]
48. Candolfi M, Curtin JF, Yagiz K, Assi H, Wibowo MK, Alzadeh GE, et al. B cells are critical to T-cell-mediated antitumor immunity induced by a combined immune-stimulatory/conditionally cytotoxic therapy for glioblastoma. Neoplasia 2011;13:947–60 [PubMed: 22028620]
49. Talhouk A, Derocher H, Schmidt P, Leung S, Milne K, Gilks CB, et al. Molecular Subtype Not Immune Response Drives Outcomes in Endometrial Carcinoma. Clin Cancer Res 2019;25:2537–48 [PubMed: 30523022]
50. Conejo-Garcia JR, Biswas S, Chaurio R. Humoral immune responses: Unsung heroes of the war on cancer. Semin Immunol 2020;49:101419 [PubMed: 33183950]
51. Bruno TC. New predictors for immunotherapy responses sharpen our view of the tumour microenvironment. Nature 2020;577:474–6 [PubMed: 31965091]

SIGNIFICANCE

This study provides new insights into the crucial role of humoral immunity in human endometrial cancer, providing a rationale for designing novel immunotherapies against this prevalent malignancy.

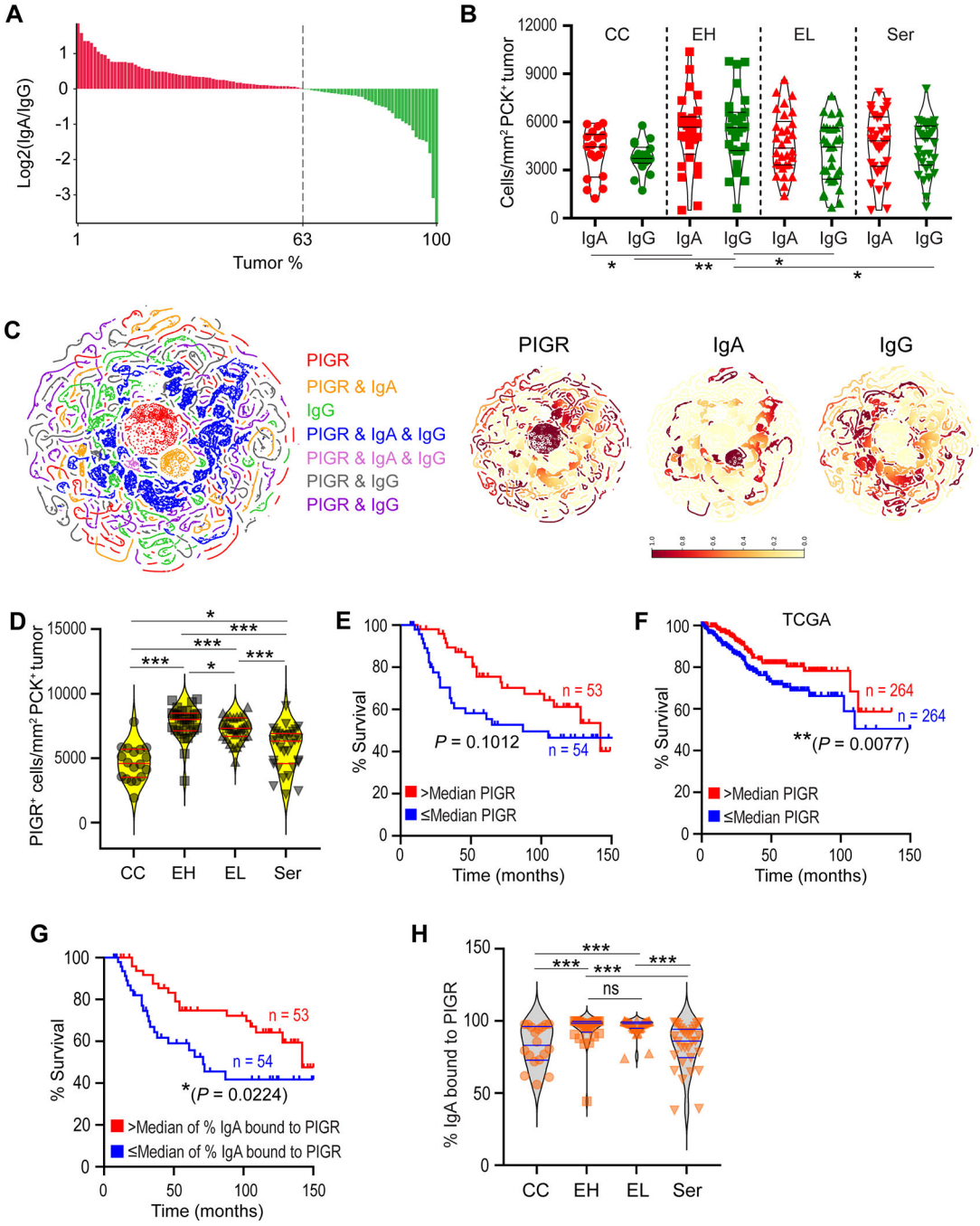

Figure 1. IgA and IgG coat pIgR$^+$ endometrial cancer cells.

(**A**) Graph showing Log2 IgA/IgG densities per tumor (%), showing 63% of all endometrial tumors have more IgA densities compared to IgG. (**B**) Densities of IgA and IgG (cells/mm^2 PCK$^+$ tumor) in pan-cytokeratin positive (PCK$^+$) cancer epithelial cells based on histology types, calculated using the number of IgA$^+$ or IgG$^+$ cells among only the PCK$^+$ cells and further normalized with unit area (mm^2) and averaged from duplicated cores. *, $P \leq 0.05$; **, $P \leq 0.01$. Unpaired two-tailed Mann Whitney test. (**C**) *Left,* t-SNE combining all four histology types embedding of 90 thousand PCK$^+$ tumor epithelial cells highlighting

diverse antibody clusters. Each dot is a cell and colors correspond to cell types inferred by spatial neighborhood-based clustering. Unique spatial neighborhoods are characterized by spatially-distinct clusters. The proportion of PCK^+ tumor cells expressing pIgR is 23.6%, pIgR with IgA is 11.7%, pIgR with IgA and IgG is 22.4%, and pIgR with IgG is 33%. Certain clusters with the same name are differently colored because they are spatially distinct clusters. Each cell represents not only itself but also its immediate neighborhood and this is used for identifying spatial clusters or 'cellular neighborhoods'. A sample can be viewed as a collection of such cellular neighborhoods where the same functional cluster can exist in multiple spatial locations. *Right,* phenotype expression distribution in t-SNE embedded reduced space for 90 thousand PCK^+ tumor cells. Relative phenotype expression is visualized by the color bar (from yellow to red) with highest expression in red. (**D**) Densities of pIgR expression (cells/mm^2 PCK^+ tumor) in PCK^+ cancer epithelial cells based on histology types, calculated using the number of $pIgR^+$ cells among only the PCK^+ cells and further normalized with unit area (mm^2) and averaged from duplicated cores. *, $P \leq 0.05$; ***, $P \leq 0.001$. Unpaired two-tailed Mann Whitney test. (**E**) Survival outcome associated with the density of $pIgR^+$ cells (averaged from duplicated cores, normalized by unit PCK^+ tumor area) in tumor islets (threshold, median; $P = 0.1202$). Two-sided log-rank (Mantel–Cox) test. (**F**) Survival outcome associated with the expression of *PIGR* mRNA in 528 annotated endometrial cancers in TCGA UCEC datasets (threshold, median; $P = 0.0077$). **, $P \leq 0.01$, two-sided log-rank (Mantel–Cox) test. (**G**) Increased percentages of total IgA bound with pIgR per PCK^+ tumor islet area (averaged from duplicated cores) are associated with improved outcome (threshold, median; $P = 0.0224$). *, $P \leq 0.05$, two-sided log-rank (Mantel–Cox) test. (**H**) Percentages of total IgA bound with pIgR per PCK^+ tumor area (averaged from duplicated cores) based on histology types. ***, $P \leq 0.001$; ns, not significant, $P > 0.05$. Unpaired two-tailed Mann Whitney test. CC, clear cell endometrial cancer; EH, endometrioid type high grade (grade 3) endometrial cancer; EL, endometrioid type low grade endometrial cancer; Ser, Serous endometrial cancer.

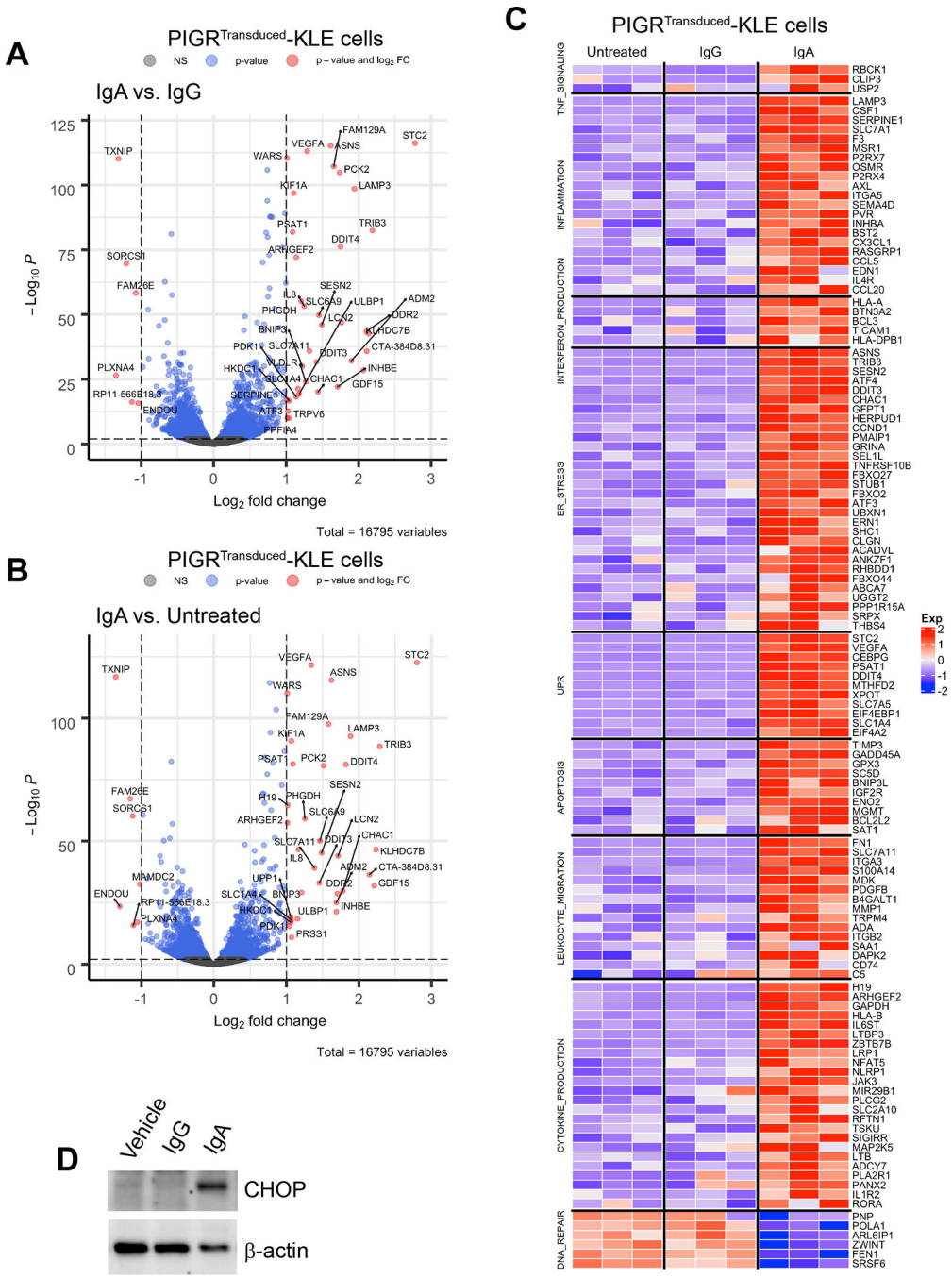

Figure 2. pIgR-dependent IgA signaling drives genome-wide transcriptional changes in endometrial cancer cells.

(**A-B**) Volcano plots showing differential analysis results for comparisons between IgA- and IgG-treated (A) or between IgA-treated and untreated (**B**) pIgR^{+} KLE cells. The cutoff for significance is FDR adjusted p-value <0.05 and log2FC>1 or log2FC< −1. (**C**) Pre-ranked gene-set enrichment analysis (GSEA), showing the top upregulated gene sets in pIgR^{transduced} KLE cells treated with irrelevant IgA compared to IgG or untreated cells

(n = 3), Kolmogorov–Smirnov test. (**D**) Western blot showing induced CHOP (DDIT3) expression in pIgR^{transduced} KLE cells upon IgA, but not IgG, treatment.

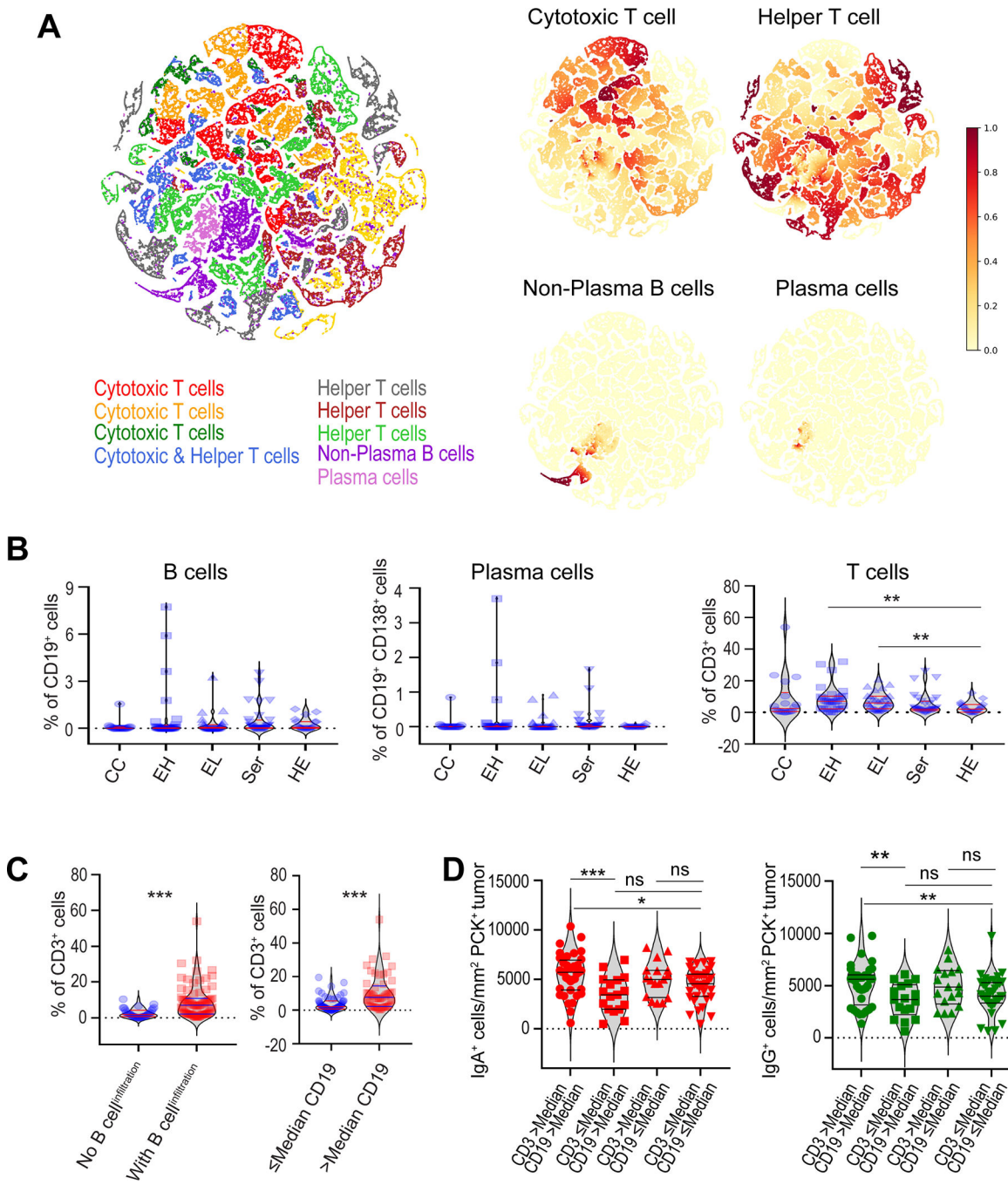

Figure 3. Concurrent B cell and T cell infiltration is associated with increased IgA and IgG densities at endometrial tumor beds.

(**A**) *Left,* t-SNE embedding of 84 thousand cells highlighting diverse T-cell and B-cell clusters. Each dot is a cell and colors correspond to cell types inferred by spatial neighborhood-based clustering. Unique spatial neighborhoods are characterized by spatially-distinct T-cell and B-cell clusters. The proportion of cytotoxic T cells is 34.2%, helper T cells is 40.5%, plasma cells is 5%, and B cells is 10%. Certain clusters with the same name are differently colored because they are spatially distinct clusters. Each cell represents

not only itself but also its immediate neighborhood and this is used for identifying spatial clusters or 'cellular neighborhoods'. A sample can be viewed as a collection of such cellular neighborhoods where the same functional cluster can exist in multiple spatial locations. *Right*, Phenotype expression distribution in t-SNE embedded reduced space for 84 thousand cells. Relative phenotype expression is visualized by the color bar (from yellow to red) with highest expression in red. (**B**) Violin plots showing percentages of $CD19^+$ B cells (*left*), $CD19^+CD138^+$ plasma cells (*middle*), and $CD3^+$ T cells (*right*) in different histology types of endometrial cancer. (**C**) Percentages of $CD3^+$ T cells is significantly higher in tumors with B cell infiltration (*left*), and tumors with higher (median threshold) B cell infiltration have significantly higher T cell infiltration (*right*). (**D**) Densities of IgA-coated (*left*) and IgG-coated (*right*) PCK^+ tumor cells, calculated using the number of IgA^+ or IgG^+ cells among only the PCK^+ cells and further normalized with unit area (mm^2) and averaged from duplicated cores, according to the median of percentages of $CD19^+$ B cell and $CD3^+$ T cell infiltrations. *, $P \leq 0.05$; **, $P \leq 0.01$; ***, $P \leq 0.001$; ns, not significant, $P > 0.05$. Unpaired two-tailed Mann Whitney test. CC, clear cell endometrial cancer; EH, endometrioid type high grade (grade 3) endometrial cancer; EL, endometrioid type low grade endometrial cancer; Ser, Serous endometrial cancer; HE, healthy endometrium.

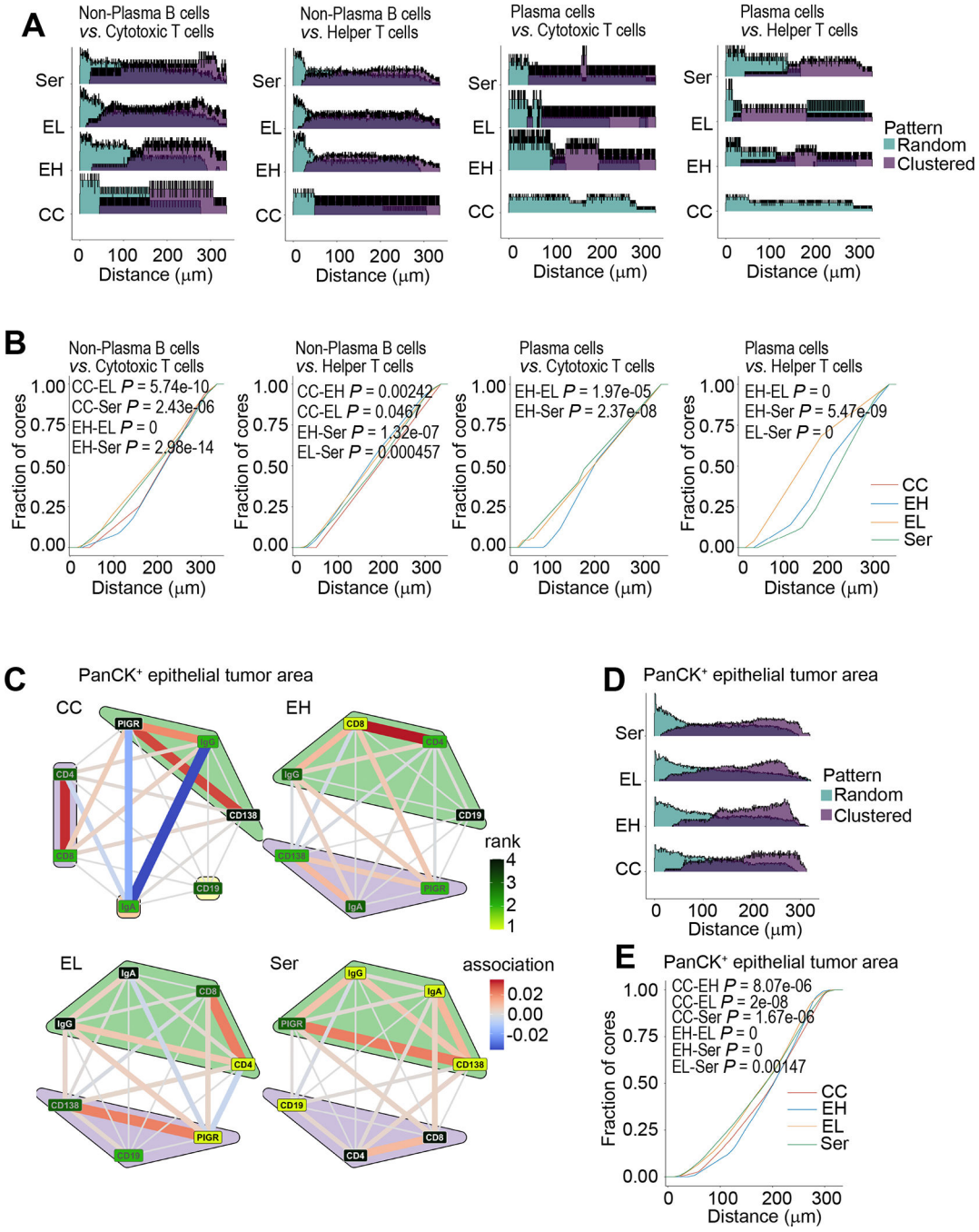

Figure 4. Spatial association between B cells, T lymphocytes and antibody coated pIgR$^+$ tumor cells depends on the histological subtype of endometrial carcinoma.

(**A**) Histogram of observed spatial patterns between non-plasma B cells and cytotoxic T cells, non-plasma B cells and helper T cells, plasma cells and cytotoxic T cells, or plasma cells and helper T cells at varying distances, as measured using the cross-type L-function. The height of each bar indicates how many cores exhibited the spatial pattern (random or clustered) at each radius for each histological type. (**B**) Empirical cumulative distribution function of the distances at which clustering between non-plasma B cells and cytotoxic

T cells, non-plasma B cells and helper T cells, plasma cells and cytotoxic T cells, or plasma cells and helper T cells was observed. The Kolmogorov-Smirnov test was used to determine if there was a significant difference in the distribution of clustering radii among the different histology types. (**C**) Averaged spatial association networks of each histology type in PCK^+ tumor area. The color and width of each edge in the network represents the spatial association, with reds indicating clustering, and blues indicating the markers are found in different areas. The color of each node reflects the ranked average quadrat count, across histological type: 1 (yellow) indicates the histological type has the highest average cell density (i.e. quadrat count), while 4 (black) means the histological type has the lowest cell density.. Polygons around collections of markers indicate that the markers are part of a spatial “community” or niche, found using the Leiden community detection algorithm. (**D**) Histogram of observed spatial patterns between IgA and pIgR at varying distances in PCK^+ tumor area, as measured using the cross-type L-function. The height of each bar indicates how many cores exhibited the spatial pattern (random or clustered) at each radius for each histological type. (**E**) Empirical cumulative distribution function of the distances at which clustering between IgA and pIgR was observed in PCK^+ tumor area. The Kolmogorov-Smirnov test was used to determine if there was a significant difference in the distribution of clustering radii among the different histology types. CC, clear cell endometrial cancer; EH, endometrioid type high grade (grade 3) endometrial cancer; EL, endometrioid type low grade endometrial cancer; Ser, Serous endometrial cancer.

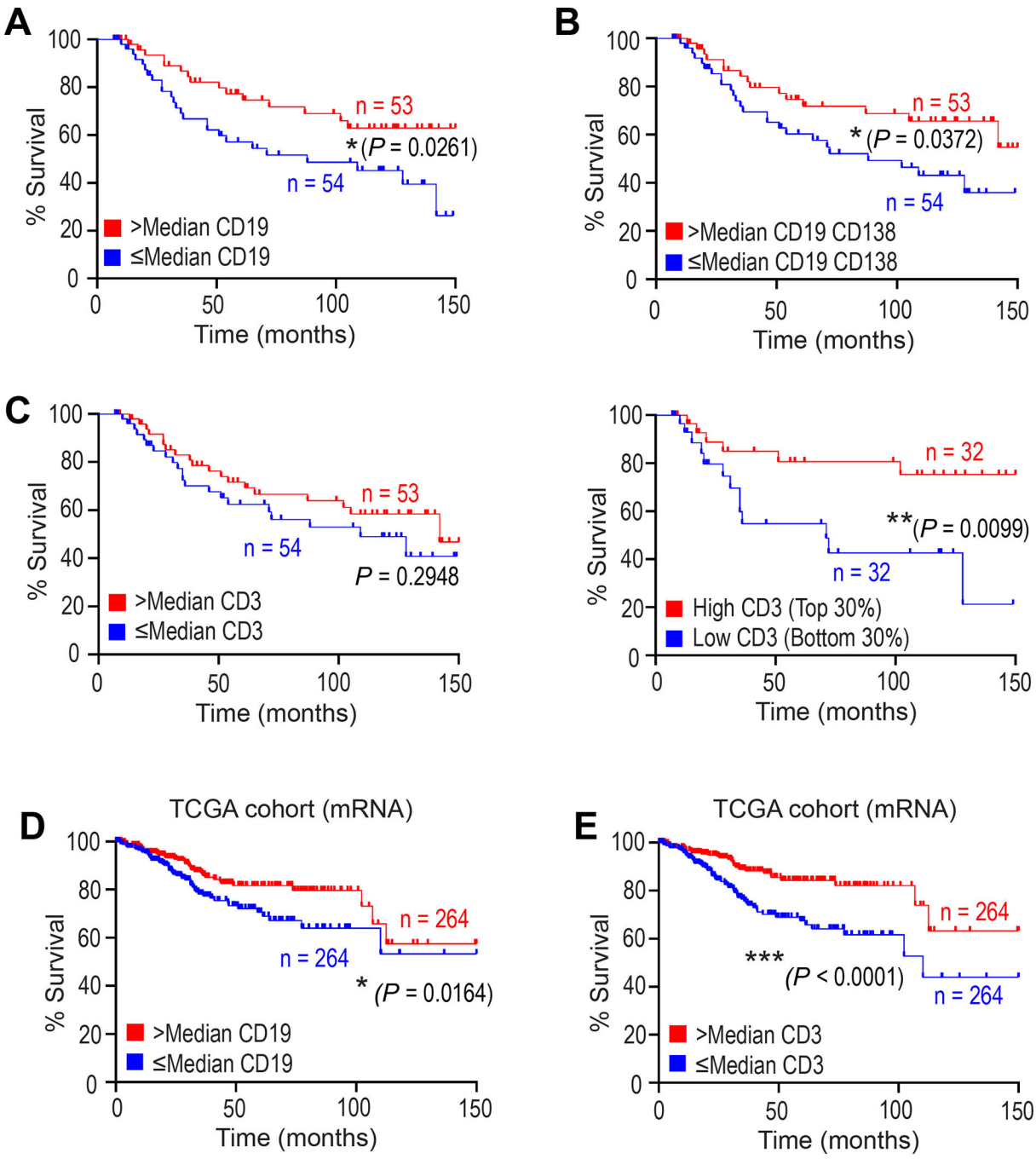

Figure 5. Concurrent T, B and plasma cell infiltration is associated with improved survival in endometrial cancer.

(**A**) Percentage of $CD19^+$ B cells (averaged from duplicated cores) is associated with improved outcome (threshold, median; $P = 0.0261$). *, $P \leq 0.05$, two-sided log-rank (Mantel–Cox) test. (**B**) Percentage of $CD19^+$ $CD138^+$ plasma cells (averaged from duplicated cores) is associated with improved outcome (threshold, median; $P = 0.0372$). *, $P \leq 0.05$, two-sided log-rank (Mantel–Cox) test. (**C**) Percentage of $CD3^+$ T cells (averaged from duplicated cores) is associated with improved outcome (*left*, threshold, median; $P =$

0.2948; *right*, threshold highest/lowest 30%; $P = 0.0099$). **, $P \leq 0.01$, two-sided log-rank (Mantel–Cox) test. (**D**) Survival outcome associated with the expression of CD19 (pan B cell marker) mRNA in 528 annotated endometrial cancer in TCGA UCEC datasets (threshold, median; $P = 0.0164$). *, $P \leq 0.05$, two-sided log-rank (Mantel–Cox) test. (**E**) Survival outcome associated with the expression of CD3 mRNA in 528 annotated endometrial cancer in TCGA UCEC datasets (threshold, median; $P < 0.001$). ***, $P \leq 0.001$, two-sided log-rank (Mantel–Cox) test.

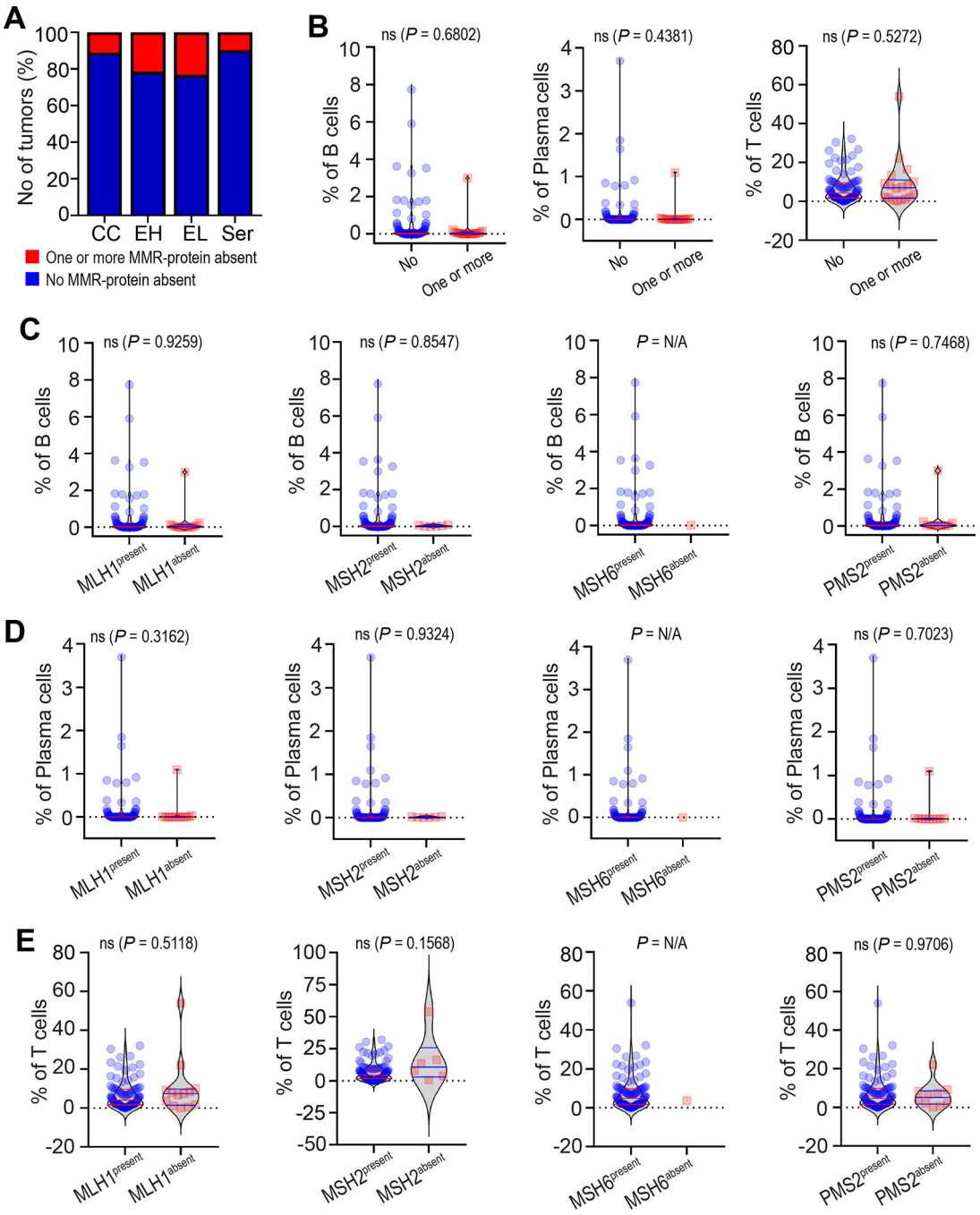

Figure 6. Defects in methyl-directed mismatch repair (MMR) protein expression in endometrial cancer do not predict lymphocyte infiltrates.

(**A**) Bar graphs showing number of tumors in each histology type of endometrial cancer with (*red color*) or without (*blue color*) defects in one or more of the four MMR gene expression, MLH1, MSH2, MSH6 and PMS2, converted to percentages. CC, clear cell endometrial cancer; EH, endometrioid type high grade (grade 3) endometrial cancer; EL, endometrioid type low grade endometrial cancer; Ser, Serous endometrial cancer. (**B**) $CD19^+$ B cell (*left*), $CD19^+CD138^+$ plasma cells (*middle*), and $CD3^+$ T cell (*right*) infiltrations compared in

tumors with and without defects in one or more of the four MMR gene expressions. ns, not significant, $P > 0.05$. (**C**) $CD19^+$ B cell infiltrations compared in tumors with and without expression of MLH1, MSH2, MSH6 and PMS2. ns, not significant, $P > 0.05$. N/A, not applicable (statistics not feasible due to single data point in the $MSH6^{absent}$ group). (**D**) $CD19^+CD138^+$ plasma cell infiltrations compared in tumors with and without expression of MLH1, MSH2, MSH6 and PMS2. ns, not significant, $P > 0.05$. N/A, not applicable. (**E**) $CD3^+$ T cell infiltrations compared in tumors with and without expression of MLH1, MSH2, MSH6 and PMS2. ns, not significant, $P > 0.05$. N/A, not applicable. Unpaired two-tailed Mann Whitney test.

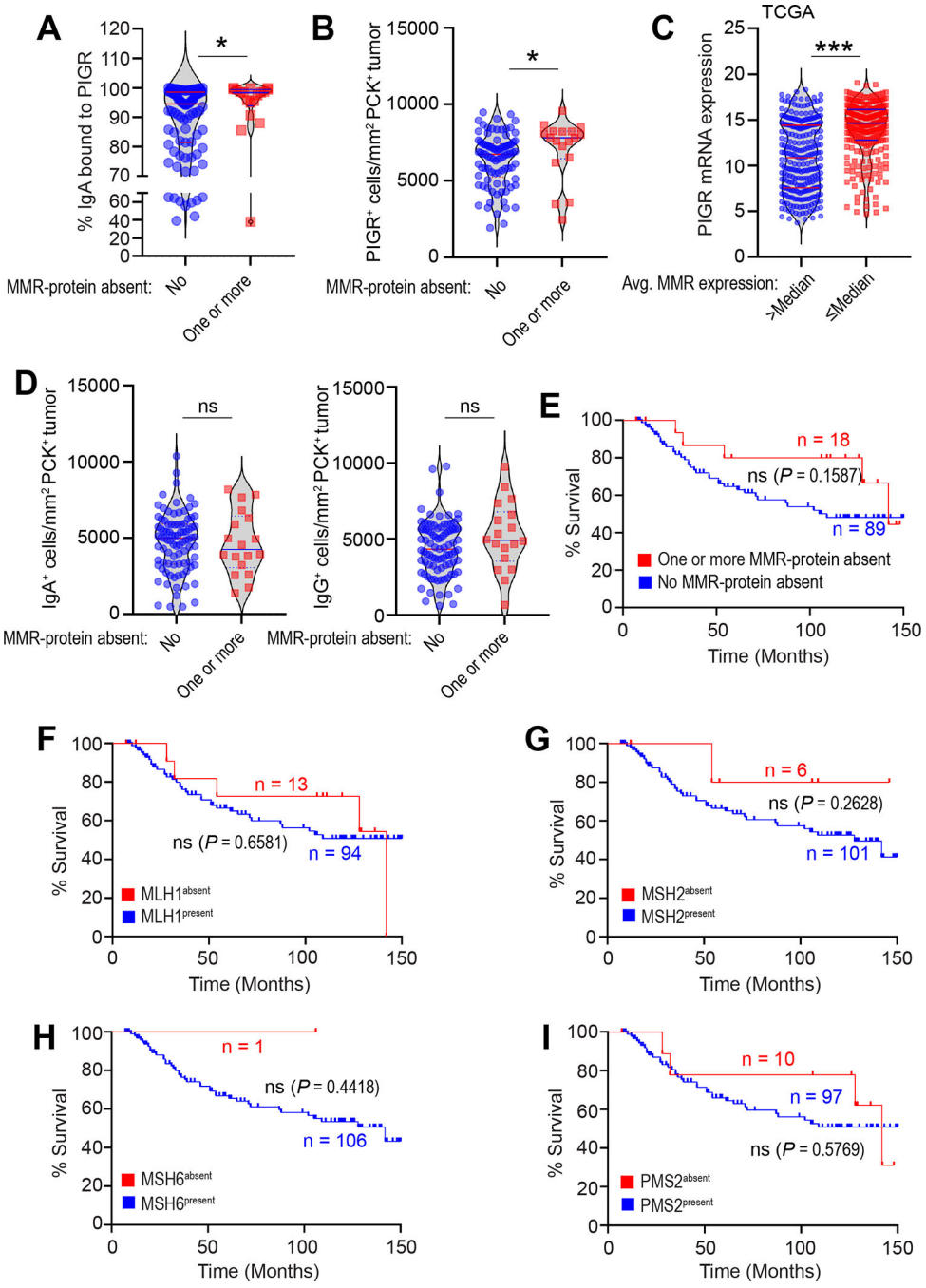

Figure 7. Defects in MMR protein expression is associated with IgA:pIgR interactions.

(**A**) Violin plot showing percentage of total IgA bound with pIgR in PCK$^+$ tumor area is significantly higher when one or more of the four MMR gene expression is absent. Unpaired two-tailed Mann Whitney test. *, $P \leq 0.05$. (**B**) Violin plot showing density of pIgR in PCK$^+$ tumor area is significantly higher when one or more of the four MMR gene expression is absent. Unpaired two-tailed Mann Whitney test. *, $P \leq 0.05$. (**C**) Violin plot showing TCGA *PIGR* mRNA level is significantly higher in tumors with MMR gene expression ≤ median. Unpaired two-tailed Mann Whitney test. ***, $P \leq 0.001$. (**D**) Violin plot showing

differences in the density of IgA^+ cells (*left*) and IgG^+ cells (*right*) in PCK^+ tumor area are not significant when one or more of the four MMR gene expression is absent. Unpaired two-tailed Mann Whitney test. ns, not significant, $P > 0.05$. (**E**) Survival analysis with or without defects in one or more of the four MMR protein expression. $P = 0.1587$; two-sided log-rank (Mantel–Cox) test. (**F**) Survival analysis according to absence of MLH1 expression. $P = 0.6581$; two-sided log-rank (Mantel–Cox) test. (**G**) Survival analysis according to absence of MSH2 expression. $P = 0.2628$; two-sided log-rank (Mantel–Cox) test. (**H**) Survival analysis according to absence of MSH6 expression. $P = 0.4418$; two-sided log-rank (Mantel–Cox) test. (**I**) Survival analysis according to absence of PMS2 expression. $P = 0.5769$; two-sided log-rank (Mantel–Cox) test.

Table 1.

Clinicopathological information summary of tissue specimens used.

Characteristics	Number of samples
Endometrial cancer tissues	
Total	107
Age (median and range)	65 (27–92)
Vital Status	
Dead	67
Alive	40
Stage	
I	52
II	8
III	29
IV	6
Unknown	12
Grade	
1 (Well Differentiated)	15
2 (Moderately Differentiated)	16
3 (Poorly Differentiated)	46
Unknown	30
Histology Subtype	
Clear Cell	18
Endometrioid Type High Grade	28
Endometrioid Type Low Grade	30
Serous	31
Control Tissues	
Healthy Endometrium	20
Control Tonsil	2
Control Lymph Node	2
Control IDC Breast	2
Control Colon Adenocarcinoma	2
Control Lung Adenocarcinoma	2